Pergamon

Heat transfer in high-temperature liquid jets

M. CHACHA, R. OCCELLI and L. TADRIST

Institut Universitaire des Systèmes Thermiques Industriels, CNRS UA 1168 Université de Provence,
Centre de Saint Jérôme, Case 162, Avenue Escadrille Normandie Niemen,
13397 Marseille Cedex 20, France

Abstract—This study focuses on the hydrodynamics and heat transfer of a very high temperature liquid jet moving through air. The purpose was to determine the velocity and temperature fields in a jet of molten materials flowing from a furnace into casting devices. Understanding hydrodynamic and heat transfer properties of the jet is essential in controlling the flow and the solidification of molten products. The non-linear equations that govern this physical problem were solved numerically using a finite-difference method applied to a laminar and axisymmetric flow with no fluctuation of the interface between the liquid jet and the continuous phase. The exit velocity profile was analyzed in terms of its effect on liquid jet hydrodynamics and cooling properties; and the Peclet number and jet emissivity in terms of their influence on the thermal exchange. In addition to the theoretical approach, experimental values were provided to validate the numerical model. Jet diameter and surface temperature profile values were measured and compared. The numerically analyzed jet diameter contraction and surface temperature values were consistent with those obtained experimentally.

INTRODUCTION

The study of liquid jets has proven itself essential to the understanding of the fundamental problems encountered in the industrial application of jet flows; the dispersion of one liquid in another is encountered in a number of situations (e.g. chemical, thermal and mechanical engineering industries).

Liquid jets have also been used in a number of rheological studies: the development of techniques for measuring normal stress in polymer solutions [1], stress relaxation in polymer solutions [2, 3] and superficial tension [4]. In most situations, the jet is formed by a fluid flowing through an orifice or a tube. At the exit, its shape, velocity and temperature profiles are altered by stress relaxation.

A number of authors have conducted major theoretical and experimental studies on the flow of a liquid in another fluid (liquid or gas) at the normal temperature [5–9]. These works deal with the assessment of characteristic quantities such as velocity profiles or the evolution of the jet diameter. Different approaches and simplifications have been proposed: some use a constant velocity value in any given cross-section of the jet [10, 11], most likely the case for very dense and highly-viscous liquids, and others divide the jet into a series of small cylinders. Duda and Vrentas [12] proposed a new coordinate frame to locate the position of the interface with a steady flow. This made it possible to determine hydrodynamic variables using boundary-layer type approximations to develop simplified momentum equations. Using this approach, several authors have proposed solutions for liquid–liquid and liquid–gas systems [13–15]. The contraction

of the liquid jet has since received experimental validation [8, 14, 15].

So far, there have been few studies on liquid jets not at normal temperature. Certain authors, such as Donnelly and Weinberger [10], Fisher and Denn [16] and Chang *et al.* [11], have worked on isothermal jets. Griffith [17] and Matovich and Pearson [18] studied the non-isothermal aspects in the production of fibers. This work has been pursued by Shah and Pearson [19] and Pearson and Shah [20]. These authors worked under the assumption that the temperature was constant in a given cross-section of the jet. Radev *et al.* [21] developed a numerical method for heat and mass transfer problems in low-temperature laminar jets found in immiscible liquid–liquid systems.

The present paper focuses on the study of the mechanical and thermal behavior of a high-temperature liquid jet flowing into another immiscible fluid. Possible applications include industrial processes such as casting, atomization and spinning in which a liquid is decanted from furnaces into devices for the production of fibers, marble and molded items. These processes involve considerable heat transfer between the hot jet and the ambient medium, and progressive cooling occurs throughout the jet. In fiber production or atomization, the size of the particle is determined primarily by the diameter and the temperature of the jet at the breakup point. A thorough understanding of the thermal dynamics and hydrodynamics in a high-temperature jet would lead to improved control of dispersion techniques.

The present study focused on the gravity flow of a high-temperature liquid moving through a circular orifice. The flow was steady and the jet was assumed

NOMENCLATURE

a, b	constants
Cp	heat capacity of the jet [J kg^{-1} K^{-1}]
E	energy of activation of the jet [J mol^{-1}]
F	unknown (U_1, U_2, V_1, V_2, R or T_2)
Fr	Froude number, $U_N^2/(2gR_N)$
g	gravity constant, 9.81 m s^{-2}
$\mathbf{i}$	radial unit vector
$\mathbf{k}$	axial unit vector
$\mathbf{n}$	normal vector pointing away from the jet surface
N_j	modified Froude number, $(1 - \rho_1/\rho_2)^* Re_2/Fr$
P	dimensionless pressure, $P^*/(\rho_2 U_N^2)$
P^*	pressure [Pa]
Pe	Peclet number, $Pe_2 = 2U_N R_N/\chi = \tau_{th}/\tau_{ec}$
Pr	Prandtl number, $Pr_2 Pe_2/Re_2$
r	dimensionless radial coordinate, r^*/R_N
r^*	radial coordinate [m]
R	dimensionless jet radius, R^*/R_N
R^*	jet radius [m]
Re	Reynolds number, $Re_2 = (2\rho_2 U_N R_N)/\mu_2$ and $Re_1 = (2\rho_1 U_N R_N)/\mu_1$
R_g	gas constant, 2 cal mol^{-1} K^{-1}
R_N	nozzle radius [m]
T	dimensionless temperature, T^*/T_N
T^*	temperature [K]
T_N	exit mean temperature [K]
U	dimensionless axial component of velocity, U^*/U_N
U^*	axial component of velocity [m s^{-1}]
U_N	exit mean velocity [m s^{-1}]
V	dimensionless radial component of velocity, V^*/U_N

V^*	radial component of velocity [m s^{-1}]
We	Weber number, $(\rho_2 U_N^2 D_N)/\sigma_{12}$
z	dimensionless axial coordinate, z^*/R_N
z^*	axial coordinate [m].

Greek symbols

ε	emissivity
θ	angular coordinate
κ	thermal conductivity of the jet [W m^{-1} K^{-1}]
μ	dynamic viscosity [Pa s]
ξ	dimensionless axial coordinate, z
ρ	density [kg m^{-3}]
σ	Stefan–Boltzmann constant, 5.67×10^{-8} W m^{-2} K^{-4}
σ_{12}	interfacial tension [N m^{-1}]
τ_{ec}	flow characteristic time [s]
τ_{th}	thermal characteristic time [s]
Φ_{rad}	radiative heat flux
χ	thermal diffusivity of the jet, $\kappa/(\rho_2 Cp)$ [m^2 s^{-1}]
ψ	stream function.

Subscripts

1	relative to the continuous phase
2	relative to the jet phase
i	relative to the radial direction
j	relative to the axial direction
∞	to infinity.

Notations

D/Dt	total derivative
$\partial/\partial t$	local derivative
$\partial/\partial x$	partial derivative with respect to x
$\vec{\nabla}$	operator nabla.

to be an opaque, gray, diffuse body in a large enclosure. The jet was also assumed to be free of internal heat sources and forming a continuum of liquid with a regular surface over the length under study (Fig. 1). Its viscosity and thermal conductivity were assumed to be constant during the process. Both fluids were assumed to be Newtonian, immiscible and incompressible. The jet retained its axisymmetrical aspect for flow conditions with a Reynolds number of less than 1000.

The evolution of velocity and temperature fields, as well as jet contraction, are obtained by numerically resolving balance equations that use a boundary layer approximation. The numerically-calculated jet radius and surface temperature values are compared with the experimental results obtained using photographic and infra-red techniques.

PHYSICAL MODEL

The configuration under study consisted of molten materials being poured under steady laminar conditions.

This system included two phases: a highly viscous liquid (i.e. the pouring jet) and a relatively non-viscous gas or continuous phase (i.e. air). The continuous phase will, however, be considered as a viscous phase in order to retain a scheme general enough to be applied to the hydrodynamics of liquid–fluid systems. The thermal aspects have been limited to liquid–gas systems.

With molten jets flowing through air, the Peclet number Pe (i.e. the ratio of thermal time to flow time) is found to be approximately 10^4, depending on exit conditions. The characteristic flow time is insignificant
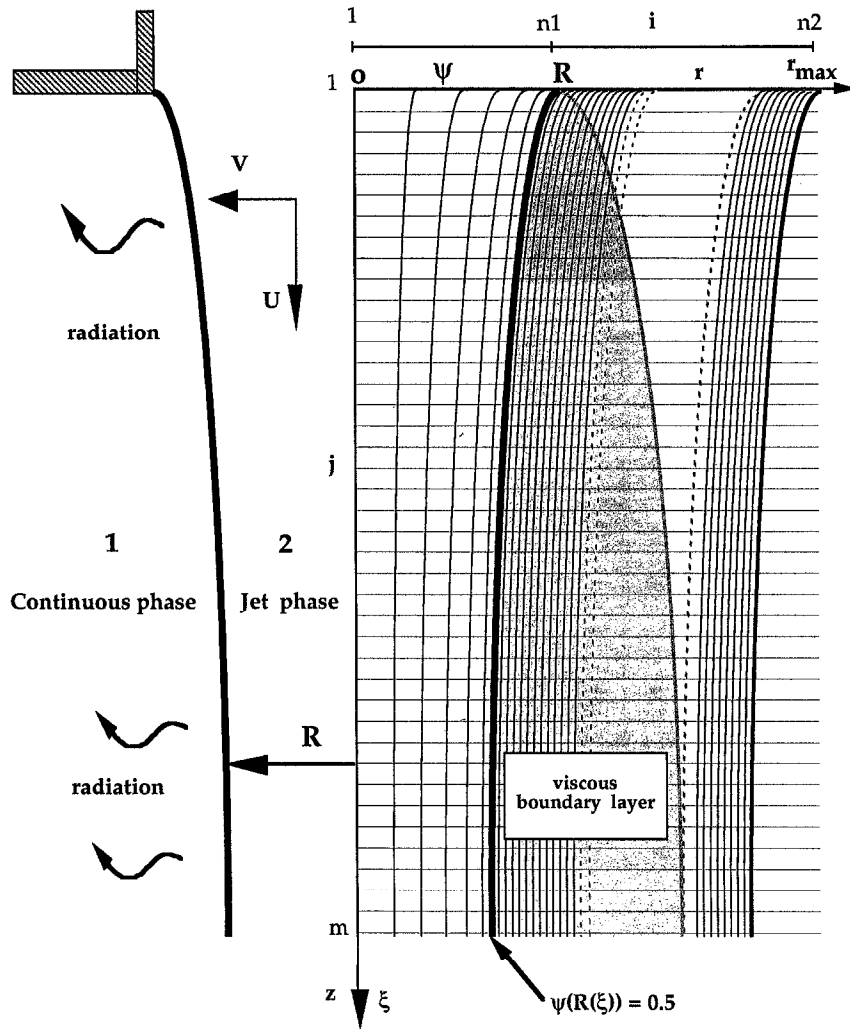
Fig. 1. Physical model of the decantation process and mesh representation.

compared to that of heat diffusion. In such conditions temperature variations are expected to be most pronounced near the surface of a jet with isothermal exit conditions.

The viscosity of molten materials is often determined by their temperature. The dynamic viscosity of these fluids is expressed using an exponential law (see Appendix) similar to those given in refs. [22, 23]. These molten products are generally poured at a temperature of approximately 2000°C and reach the casting devices before they have solidified (solidification occurs at about 1800°C). In this range, the viscosity of the jet varies by a factor of nearly 10. In such conditions the continuous phase is gaseous and the viscosity ratio μ_1/μ_2 is nearly constant (close to zero). Variations therefore have little significant influence on the velocity distribution in the jet [13, 14]. For this reason the initial viscosity value of the jet was retained throughout the decantation process.

To predict hydrodynamic and thermal behavior of the liquid jet, the flow was assumed to be steady and

the jet (an opaque, gray, diffuse body in a large enclosure) to be free of internal heat sources, forming a continuum of liquid with a regular surface over the length under study. Only radiant heat exchanges were taken into account at the jet surface. The jet retained its axisymmetrical aspect under different flow conditions (Fig. 1). Its thermo-physical properties were held constant. Both fluids were assumed to be Newtonian, immiscible and incompressible.

Equations

In accordance with these hypotheses, the system is described using mass, momentum and energy conservation equations.

The jet can be represented in a cylindrical coordinate frame, the origin of which coincides exactly with the center of the pouring orifice, and the z-axis with the pouring axis of the jet. The continuous phase is located in the same coordinate frame (Fig. 1).

The equations representative of the pouring process are made dimensionless by using characteristic quan-

tities at the nozzle: the mean velocity U_N for velocities, the mean temperature T_N for the temperature, the radius of the orifice R_N for lengths, and the quantity $\rho_2 U_N^2$ for the pressure.

For large enough Reynolds numbers, the flow field can be described accurately by means of boundary-layer type approximations; such approximations have been validated for slender jets [13–15]. This considerably simplifies the system of equations. The main direction of the flow is the same as that of the jet axis; thus: $V \ll U$ and $\partial/\partial z \ll \partial/\partial r$. The radial pressure gradient is negligible in both phases.

As the boundary is unknown, the interface cannot be located in the classical coordinate system. Duda and Vrentas [12] overcame this mathematical difficulty by introducing a protean coordinate frame, (ψ, θ, ξ) (Fig. 1). In this new coordinate system, the independent variable ψ represents the stream function (whose value is known exactly at the jet surface). Thus:

$$\frac{\partial \psi}{\partial r} = rU \quad \frac{\partial \psi}{\partial z} = -rV \quad \xi = z. \tag{1}$$

In the new coordinate system, the balance equations of the jet phase are as follows:

Momentum:

$$\frac{\partial P_2}{\partial \psi} = 0 \tag{2}$$

$$U_2 \frac{\partial U_2}{\partial \xi} = -\frac{\partial P_2}{\partial \xi} + \frac{1}{2Fr} + \frac{2}{Re_2}\left[2U_2 \frac{\partial U_2}{\partial \psi}\right.$$
$$\left. + r^2 U_2 \left(\frac{\partial U_2}{\partial \psi}\right)^2 + r^2 U_2^2 \frac{\partial^2 U_2}{\partial \psi^2}\right] \tag{3}$$

Energy:

$$U_2 \frac{\partial T_2}{\partial \xi} = \frac{2}{Pe_2}\left[2U_2 \frac{\partial T_2}{\partial \psi} + r^2 U_2 \left(\frac{\partial U_2}{\partial \psi}\right)\left(\frac{\partial T_2}{\partial \psi}\right)\right.$$
$$\left. + r^2 U_2^2 \frac{\partial^2 T_2}{\partial \psi^2}\right] \tag{4}$$

where Fr is the Froude number, Re_2 the jet phase Reynolds number, and Pe_2 the Peclet number of the jet. The following variable transformation equations are also used:

$$\frac{\partial r}{\partial \psi} = \frac{1}{rU_2} \tag{5}$$

$$\frac{\partial r}{\partial \xi} = \frac{V_2}{U_2}. \tag{6}$$

For the continuous phase:

Continuity:

$$\frac{\partial(rV_1)}{\partial r} + \frac{\partial(rU_1)}{\partial z} = 0 \tag{7}$$

Momentum:

$$V_1 \frac{\partial U_1}{\partial r} + U_1 \frac{\partial U_1}{\partial z} = \frac{2}{Re_1}\left[\frac{1}{r}\frac{\partial}{\partial r}\left(r\frac{\partial U_1}{\partial r}\right)\right] \tag{8}$$

$$\frac{\partial P_1}{\partial r} = 0 \tag{9}$$

where Re_1 is the continuous-phase Reynolds number.

Beyond the viscous boundary layer, the continuous phase is inactive; which gives

$$\frac{\rho_2}{\rho_1}\frac{\partial P_1}{\partial z} = \frac{1}{2Fr}. \tag{10}$$

Boundary conditions
At the exit ($\xi = 0$)
The velocity and temperature profiles must be defined:

In the orifice
—Either parabolic or flat velocity profiles can be used:

$$U_2^2(0, \psi) = 4(1 - 2\psi) \quad \text{or}$$

$$U_2^2(0, \psi) = 1 \quad V_2(0, \psi) = 0. \tag{11}$$

—The temperature profile is assumed to be flat in the jet:

$$T_2(0, \psi) = 1. \tag{12}$$

Adjacent to the orifice

$$U_1(0, r) = 0 \quad V_1(0, r) = 0. \tag{13}$$

At the interface
At the interface, $\psi(R) = \frac{1}{2}$. This value is obtained by expressing the mass flow rate between the exit and any other cross-section of the jet.

Equilibrium at the interface
As demonstrated by Yu and Scheele [15], the continuity of the normal and shear stresses can be reduced to

$$\mu_1 \frac{\partial U_1}{\partial r} = \mu_2 RU_2 \frac{\partial U_2}{\partial \psi} \tag{14}$$

and

$$P_2 - P_1 = \frac{2}{R\,We}. \tag{15}$$

$P_2 - P_1$ is the dimensionless pressure jump caused by the curvature of the interface. We is the Weber number.

From equations (15) and (10), the momentum equation (3) can be expressed as

$$2U_2 \frac{\partial U_2}{\partial \xi} = \frac{N_j}{Re_2} + \frac{2}{We\,R^3}\frac{\partial R^2}{\partial \xi} + \frac{4}{Re_2}$$
$$\times \left[2U_2 \frac{\partial U_2}{\partial \psi} + r^2 U_2 \left(\frac{\partial U_2}{\partial \psi}\right)^2 + r^2 U_2^2 \frac{\partial^2 U_2}{\partial \psi^2}\right]. \tag{16}$$

The dimensionless number N_j determines the buoyancy of the dispersed phase relative to the continuous phase. When N_j is greater than 1 the jet contracts and when less than 1 the jet expands [24]. The continuity

conditions of the velocity components must be satisfied; hence:

$$U_1 = U_2 \quad V_1 = V_2. \tag{17}$$

Heat exchange conditions at the interface

Radiation and convection exchanges occur at the jet surface (assumed to be opaque). Radiation reaches its highest levels with high temperature values. A simple local estimation over a cylinder shows that the convection flux is less than 1% compared to the radiation flux. In these conditions, the convection flux at the jet surface is disregarded.

In the protean coordinate frame, the heat flux conservation equation reduced to $-k\mathbf{n} \cdot \overrightarrow{\text{grad}}\, T = \Phi_{\text{rad}}$ gives

$$\left.\frac{\partial T_2}{\partial \psi}\right)_{(1/2,\xi)} = -\left[\frac{\varepsilon\sigma D_N T_N^3}{2\kappa R(aU_2 - bV_2)}\right]$$

$$\times (T_2(1/2,\xi)^4 - T_\infty^4) - \left[\frac{b}{R(aU_2 - bV_2)}\right]\left.\frac{\partial T_2}{\partial \xi}\right)_{(1/2,\xi)} \tag{18}$$

where $a = \mathbf{n} \cdot \mathbf{i}$ and $b = \mathbf{n} \cdot \mathbf{k}$.

$\mathbf{i}$ is the radial unit vector, $\mathbf{k}$ the axial unit vector, and $\mathbf{n}$ the normal vector pointing away from the jet surface. T_∞ is the temperature of the large enclosure.

At the jet axis ($\psi = 0$)

$$V_2 = 0 \quad \frac{\partial T_2}{\partial r} = 0 \quad \frac{\partial U_2}{\partial r} = 0. \tag{19}$$

At the outer edge of the boundary layer

The condition which corresponds to an immobile continuous phase located beyond the viscous boundary layer is written as

$$U_1 = 0 \quad V_1 = 0. \tag{20}$$

This condition is valid at $r \to \infty$ but can be satisfied with a sufficient degree of accuracy at an appropriate $r = r_{\max}$ ($r_{\max}$ is chosen from numerical experiments).

Numerical resolution of the system of equations

Heat and momentum equations are disassociated since both the density and the viscosity of the jet are constant; hydrodynamic quantities are determined and then used to calculate the temperature field.

The first and second derivatives are estimated using the finite-difference approach [25] on an appropriate grid whose increments are $\Delta\psi$, $\Delta\xi$ and Δr for the continuous phase (Fig. 1). This scheme is second order in (ψ, r) and implicit in ξ. Making equations (4), (8) and (16) discrete gives two three-diagonal systems of equations in T_2 and U:

$$A_i F_{i,j} + B_i F_{i+1,j} + C_i F_{i-1,j} = D_i. \tag{21}$$

The simultaneous differential equations include only first derivatives along the principal flow axis ξ. At a given ξ, the systems of equations can be solved regardless of the downstream flow quantities. Since

the velocity profile is known at $\xi = 0$, solutions are calculated step by step by solving the corresponding system along the radial axis. For U and T_2, equation (21) is solved using a three-diagonal algorithm. R, V_1 and V_2 are calculated using equations (5), (7) and (6), respectively. The calculation for each ξ is terminated whenever max (e_U, e_T, e_R, e_V) is less than 10^{-6}: $e_F = |F_{i,j}^k - F_{i,j}^{k-1}|$ and k is the kth iteration.

RESULTS

Several step sizes were used to establish independence of the numerical results from the grid and step size. All final calculations were performed using $r_{\max} \approx 10$, $\Delta\psi = 0.01$, $\Delta r = 0.01$ and $\Delta\xi \leqslant 1$, depending on the jet length. Figure 2 shows the jet radius and surface temperature profile computed using $\Delta\xi = 0.25, 0.5$ and 1. Figure 2 illustrates the numerical scheme stability. Indeed, practically no difference appears in the results.

The numerical results below correspond to the pouring of molten oxides. The jet emerges isothermally at 2200°C through a ϕ 10 mm orifice. The characteristics of the pouring liquid are presented in the Appendix. The influence of the imposed exit velocity profile, jet Reynolds number, jet emissivity and continuous-phase properties was examined.

Velocity field and jet radius

Figure 3 shows the evolution of the axial velocity along the z-axis for the liquid–gas system used in this study. The jet contraction is shown in Fig. 4. The two velocity profiles are imposed at the exit. The numerical results show that the gas phase offers negligible resistance to the jet flow. For the flat velocity profile at the exit, there is no relaxation of the velocity profile. The velocity is uniform in every cross-sectional area of the jet: the velocity profile remains flat [Fig. 3(b) and (b')]. In the case of a parabolic exit velocity profile, the relaxation is very rapid. The interfacial axial velocity becomes equal to the jet axis velocity over about $20R_N$ [Fig. (3a)].

In a liquid–liquid system, the jet has a slower velocity relief because the viscous friction at the interface is 'proportional' to the viscosity ratio μ_1/μ_2, and is greater than in liquid–air systems [14]. This is seen in Fig. (3a), where the physical properties of the continuous phase were considered to be similar to those of water. The interfacial axial velocity becomes equal to the jet axis velocity above about $50R_N$. The increase in the density ratio ρ_1/ρ_2 reduces gravity effects, resulting in even weaker jet contraction.

The difference between the curves for the two types of exit velocity profile are due to differences in the bulk velocity of the jets. In all cases, velocity profiles release over short distances, because of the rapid relaxation of stress (Fig. 3).

Although the aspect is the same for both types of profile, the jet contraction can not be identical since the exit conditions differ. The contraction is greatest

(A)

(B)
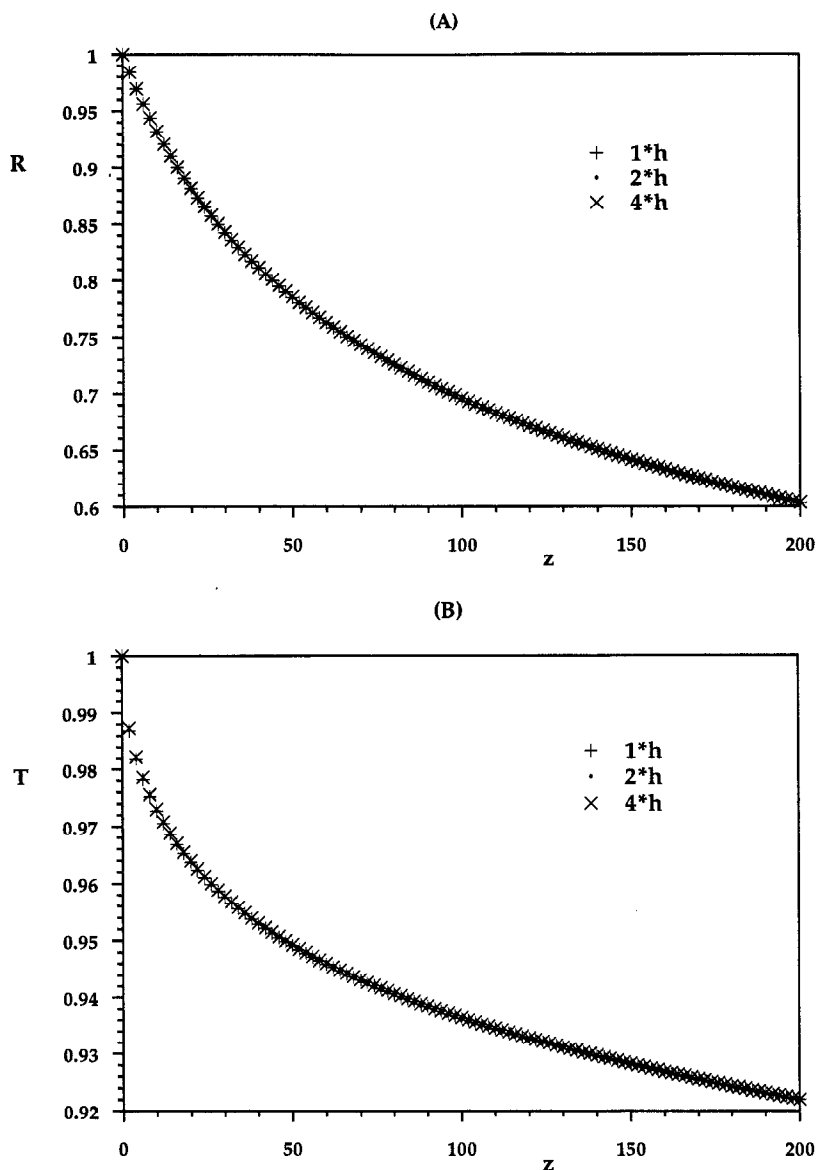
Fig. 2. Test on the step size insensitivity of the numerical scheme: $h = 0.25$ (flat exit velocity profile: $Re_2 = 100$; $Pr_2 \approx 150$; $Fr \approx 30$; $We \approx 174$). (A) Jet radius, (B) jet surface temperature.

near the exit (Fig. 4), and parabolic exit velocity profiles [Fig. 4(a) and (a')] showed greater contraction than flat profiles [Fig. 4(b) and (b')]. Further downstream, the diameter diminishes slightly. In the case of longer jets, both types of exit velocity profile tend toward a single contraction curve.

Temperature of the jet

There have been few experimental investigations of thermal profiles for high-temperature jets formed of molten materials. A theoretical approach for non-isothermal liquid jets has been proposed [18, 19, 21].

Figures 5 and 6 show the temperature variations along radial and axial coordinates, respectively. In a cross-section of the jet, the temperature decreases on

moving from the core toward the jet surface. There is a considerable temperature gradient in the region near the interface for both profile types. The temperature remains fairly constant over a large portion of the cross-section (Fig. 5). Figure 5 shows the case of a flat exit velocity profile, but the same conclusions were obtained with a parabolic profile.

The influence of the velocity profile was also analyzed in terms of the cooling along the axial direction. Assuming that velocity and temperature profiles are flat in the jet cross-section, the larger the jet diameter, the greater the cooling (as per the energy conservation equation). The parabolic exit velocity profile showed greater contraction than the flat profile. The energy conservation equation indicates that there should be
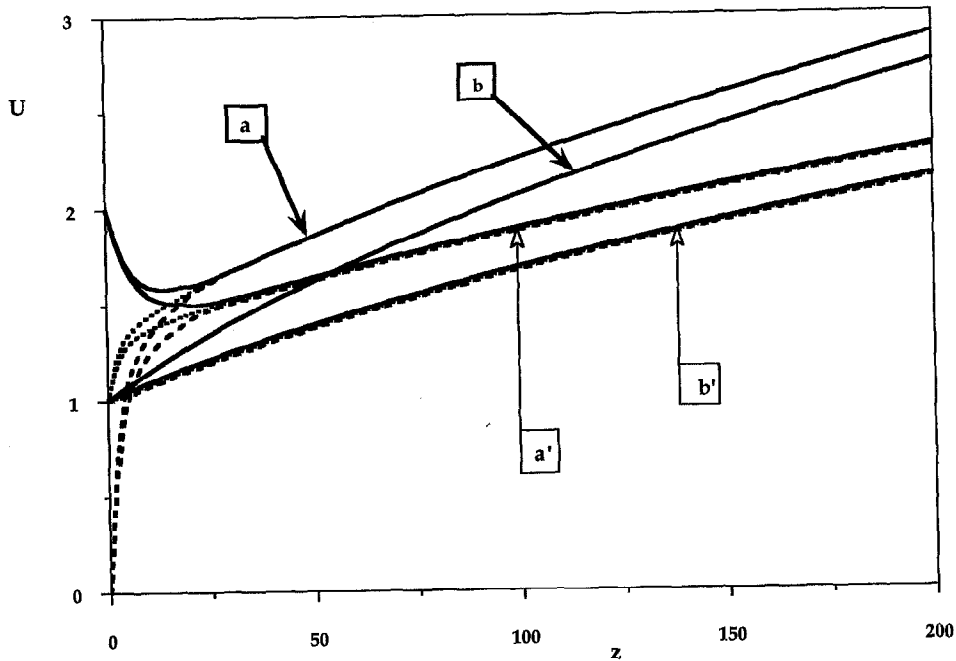
Fig. 3. Variation of the axial velocity vs z-axis: influence of the continuous phase and the jet exit velocity profile ($Re_2 = 100$; $Pr_2 \approx 150$; $Fr \approx 30$; $We \approx 174$). Parabolic exit velocity profile (a, a'); flat exit velocity profile (b, b'). (——) At the jet axis; (———) at the surface; (· · ·) jet mean velocity. Modified continuous phase: a' and b' ($\rho_1 = 1$ g cm^{-3}; $\mu_1 = 0.89 \times 10^{-2}$ p). Air: a and b.
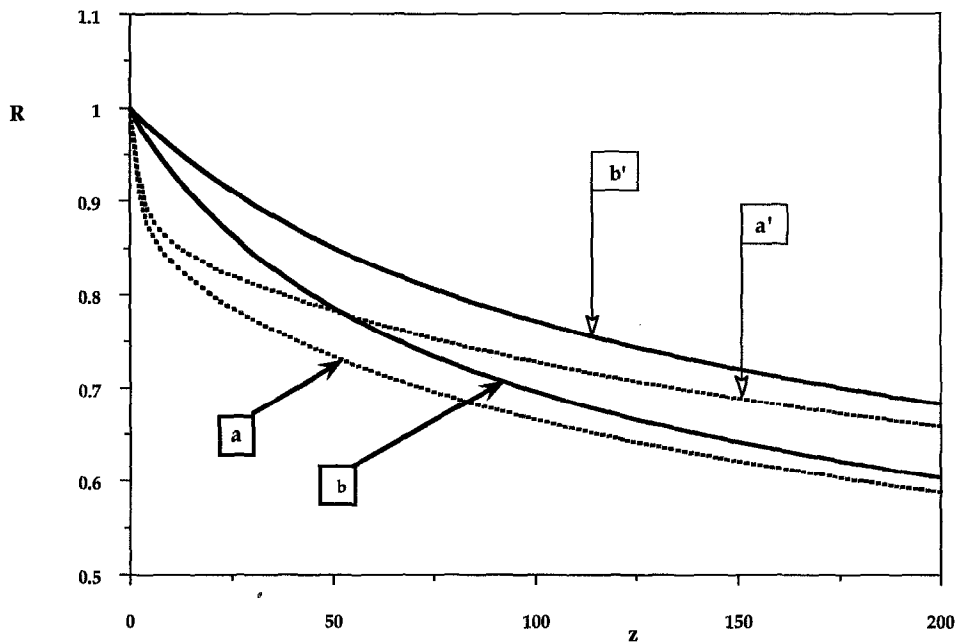
Fig. 4. Variation of the jet radius vs z-axis: influence of the continuous phase and the jet exit velocity profile ($Re_2 = 100$; $Pr_2 \approx 150$; $Fr \approx 30$; $We \approx 174$). Parabolic exit velocity profile (a, a'); flat exit velocity profile (b, b'). Modified continuous phase: a' and b' ($\rho_1 = 1$ g cm^{-3}; $\mu_1 = 0.89 \times 10^{-2}$ p). Air: a and b.

greater cooling with a flat profile. Figure 6 shows that the mean temperature of the fluid is greater for the parabolic profile. In these flow conditions, cooling and surface temperatures show virtually identical values for both profile types. In Fig. 6, the temperature can be seen to decrease by about 8% from the initial temperature at the jet surface regardless of the initial velocity profile. There is practically no decrease in the
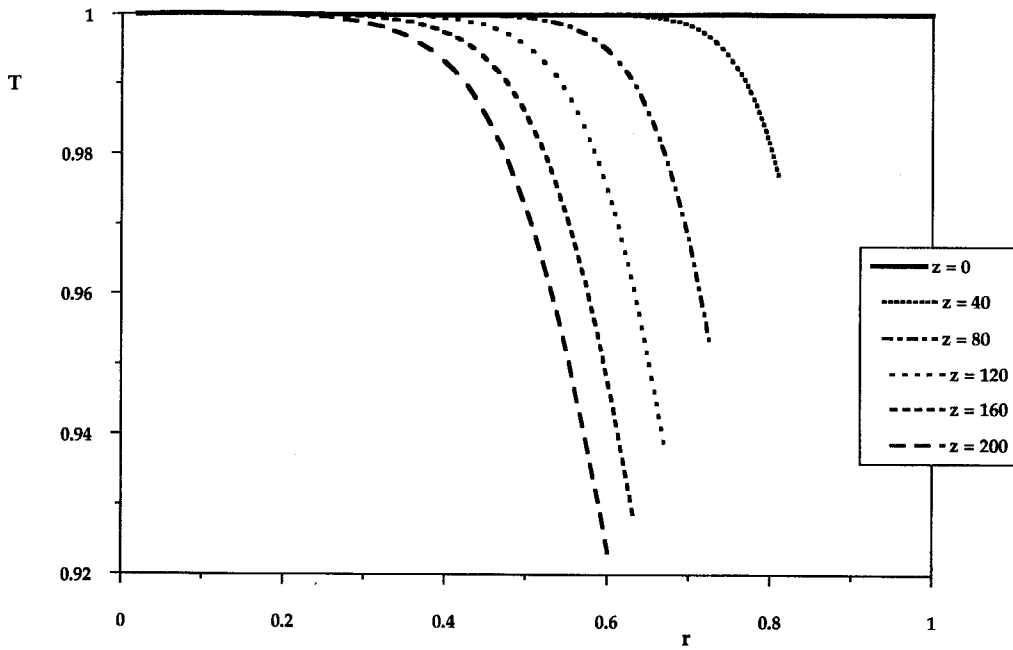
Fig. 5. Temperature profile in various cross-sections of the molten oxide jet flowing into air with a flat exit velocity profile ($Re_2 = 100$; $Pr_2 \approx 150$; $Fr \approx 30$; $We \approx 174$).
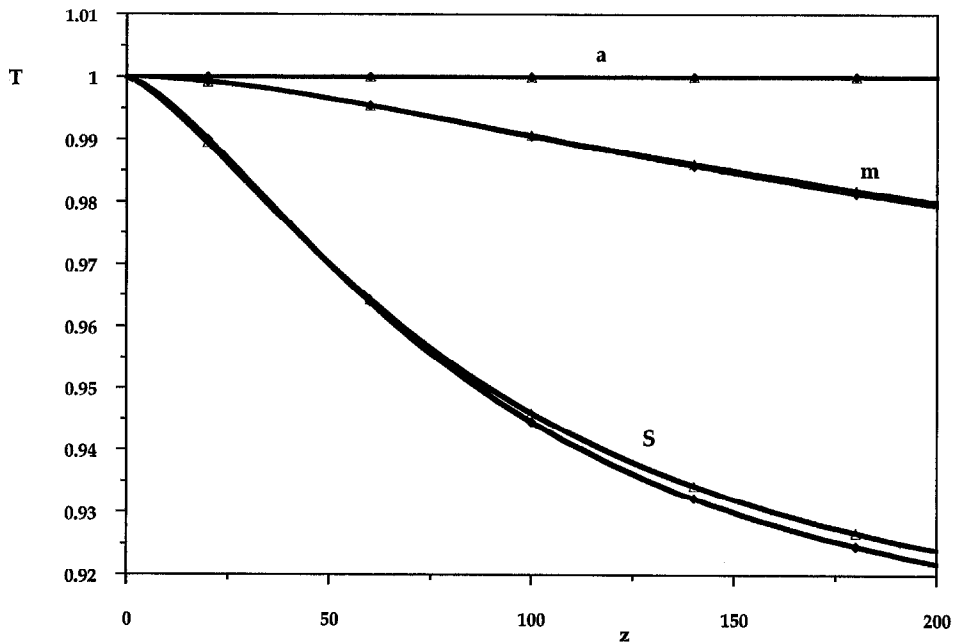
Fig. 6. Variation of the temperature of the molten oxide jet in air vs z-axis : influence of the jet exit velocity profile ($Re_2 = 100$; $Pr_2 \approx 150$; $Fr \approx 30$; $We \approx 174$). Parabolic exit velocity profile (△ —); flat exit profile (—◆—). (s) Surface temperature; (m) mean temperature; (a) axis temperature.

temperature along the jet axis (up to 1 m from the orifice). The mean temperature decrease is approximately 2% of the mean exit temperature over the same distance. The largest temperature decrease is observed near the exit. Here, the extremely hot pouring liquid is subjected to thermal shock after coming into contact with a very low temperature environment. This

cooling process is extremely abrupt. Beyond this zone (i.e. several diameters D_N), the decrease is less pronounced.

Characteristic jet parameters were analyzed for their influence on the evolution of temperature along the main flow axis. When the Reynolds number (and consequently the Peclet number) of the jet is modified

(A)

(B)
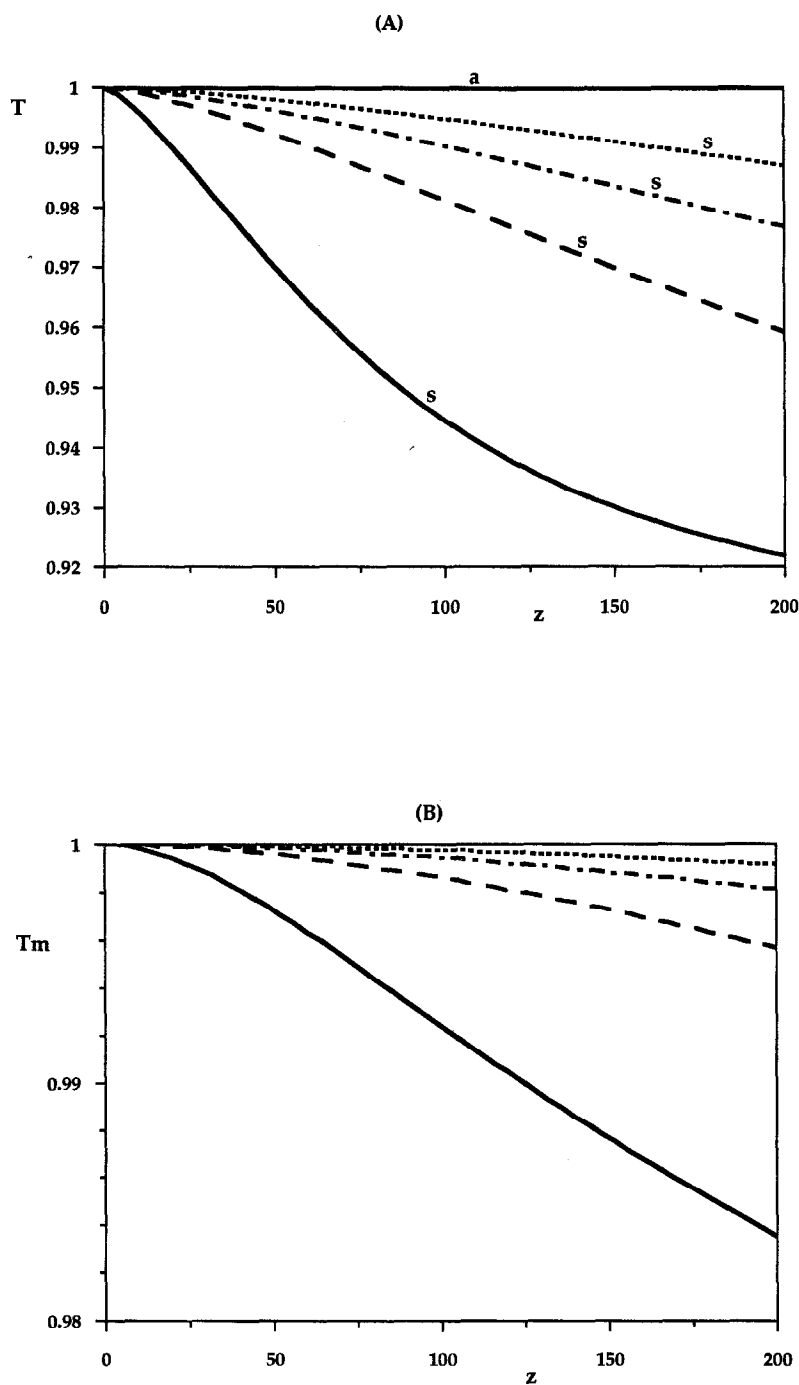
Fig. 7. Temperature variation in the molten oxide jet with a flat exit velocity profile vs z-axis : influence of jet phase Reynolds number Re_2 (or Pe_2). (———) $Re_2 = 100$; $Pr_2 \approx 150$; $Fr \approx 30$; $We \approx 174$. (— — —) $Re_2 = 300$; $Pr_2 \approx 150$; $Fr \approx 274$; $We \approx 1567$. (— ·· — ··) $Re_2 = 500$; $Pr_2 \approx 150$; $Fr \approx 760$; $We \approx 4300$. (····) $Re_2 = 800$; $Pr_2 \approx 150$; $Fr \approx 1950$; $We \approx 11\ 100$. (A) (s) Surface temperature; (a) axis temperature. (B) Mean temperature.

for a given mean exit temperature, variations of the surface [Fig. 7(A)] and mean temperature values [Fig. 7(B)] are inversely proportional to those of the Reynolds number. With large Reynolds numbers, however, the mean temperature changes slightly for a given jet length [Fig. 7(B)].

Figure 8 shows the influence of the emissivity on the axial, surface and mean temperature values. The decrease in temperature at the jet surface increases with the emissivity (up to 10% for the assumed flow conditions and an emissivity of 1). But these variations remain slight for the mean temperature (approxi-
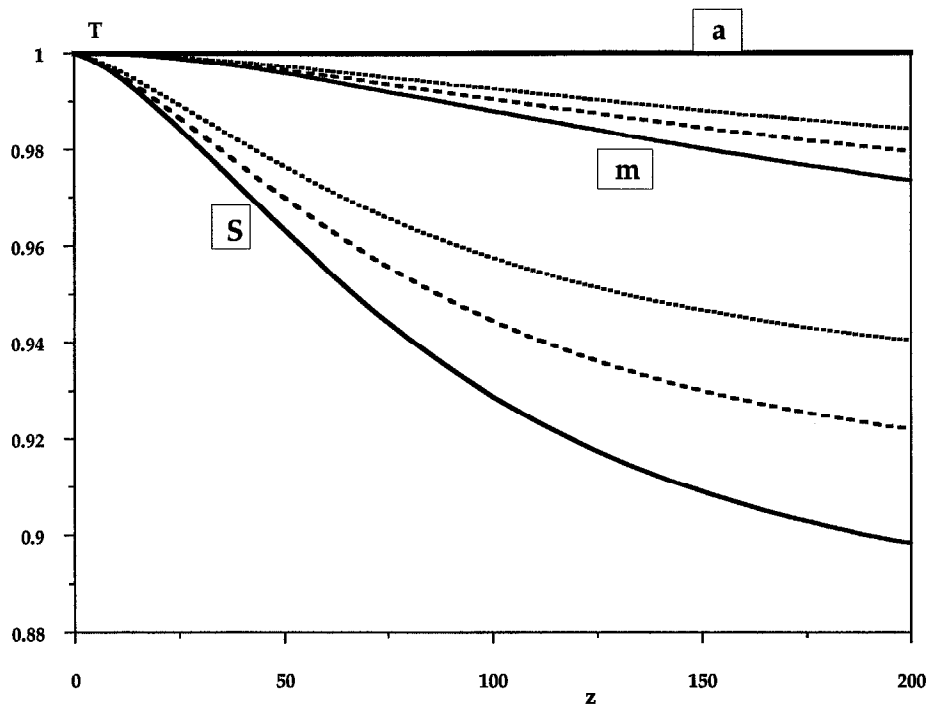
Fig. 8. Temperature variation in the molten oxide jet with a flat exit velocity profile plotted vs z-axis: influence of jet emissivity ($Re_2 = 100$; $Pr_2 \approx 150$; $Fr \approx 30$; $We \approx 174$). (s) Surface temperature; (m) mean temperature; (a) axis temperature. (———) $\varepsilon = 1$; (– – –) $\varepsilon = 0.7$; (· · ·) $\varepsilon = 0.5$.

mately 2% 1 m from the orifice for maximum emissivity).

COMPARISON OF NUMERICAL AND EXPERIMENTAL RESULTS

Numerical and experimental results for a molten oxide jet were compared in terms of contraction and the surface temperature (because of the assumed opacity of the jet). An experimental apparatus was built for this purpose, as no published experimental results could be found at these temperature levels. The experimental set-up consisted of an electric furnace in which the oxides were melted by means of graphite electrodes. The liquid obtained was then poured vertically under steady-state laminar conditions. The surface of the liquid in the melting shaft was approximately 30 cm above the injection orifice. The surface of the liquid was large enough to assume that the flow variations would be negligible during the duration of the measurements. (The flow stabilized several seconds after the initial injection.) After a steady laminar flow had developed, the acquisition system for the surface temperature and the jet diameter values was then activated. Several experiments were performed with different injection conditions (flow rate and mean injection temperature). The surface temperature of the jet was measured using an infra-red camera and a radiation pyrometer. The emissivity of the jet was

equal to 0.8 for all experiments. The diameters of the jet were measured from the photographs taken during the pouring operation [26].

Figures 9–12 represent the results for two different typical pouring operations. The measured mean exit temperatures were 2160°C for the first one and 2240°C for the second one. The injections were performed through a ϕ 14 mm orifice and a ϕ 16 mm orifice, respectively. The exit velocity profile was assumed to be flat for the numerical models. This type of profile seemed suitable as the furnace shell was not thick enough to allow a parabolic velocity profile to develop at the exit of the injection orifice. The injection orifice was a hole made through the lower part of the furnace.

Good agreement is observed between measured and calculated jet radius values (Figs. 9 and 11). The maximal relative difference $[(R_{num.} - R_{exp.})/R_{exp.}]$ is indeed less than 3%, even for a low Reynolds number (Fig. 9). At low Reynolds numbers one observes very high contraction of the jet in general; and one is near the limit of validity of boundary-layer type approximations.

The measured surface temperature decreases considerably as the jet moves from the exit of the nozzle toward the injection mold. Numerical simulation predicts this result fairly accurately, but the values differ slightly from experimental results (Figs. 10 and 12). The difference between numerical and experimental results is more pronounced in the case with lower
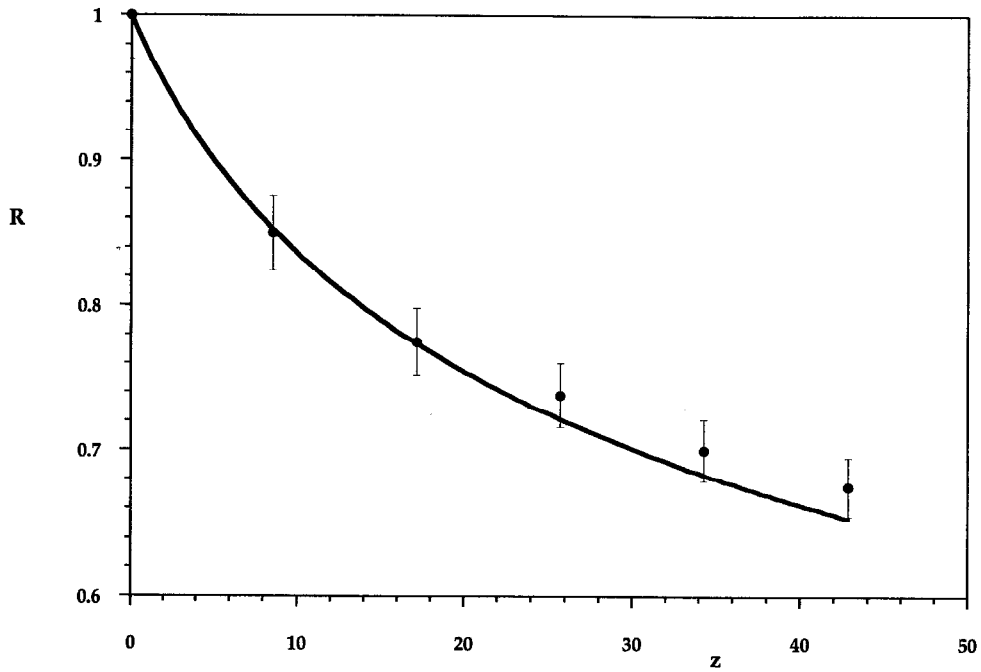
Fig. 9. Comparison in the jet contraction vs z-axis between numerical and experimental results for a pouring of molten oxides where $Re_2 \approx 60$ and $Pe_2 \approx 14\,000$ ($Fr \approx 9$; $We \approx 106$). (———) Numerical results; (●) experimental points; (◆) error bars (3%).
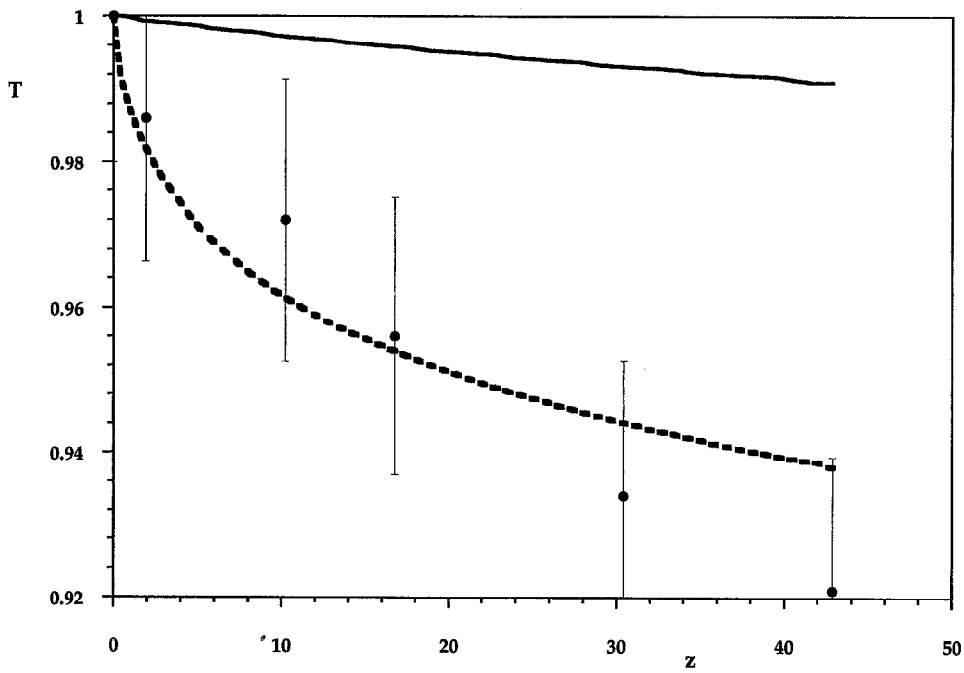
Fig. 10. Comparison in the surface temperature variation vs z-axis between numerical and experimental results for a pouring of molten oxides where $Re_2 \approx 60$ and $Pe_2 \approx 14\,000$ ($Fr \approx 9$; $We \approx 106$). Numerical model: (———) surface temperature; (———) mean temperature. (●) Experimental results; (◆) error bars (2%).

Reynolds number (or Peclet number). The maximum relative difference $[(T_2(\psi = 1/2)_{exp.} - T_2(\psi = 1/2)_{num.})/ T_2(\psi = 1/2)_{exp.}]$ is less than 2% in both cases.

The differences can be attributed to a number of factors (e.g. precision of measuring devices, falsely

assumed jet opacity, etc...). The coherence between these two approaches is, however, respected. The cooling at the surface and the contraction of the pouring jet follow laws similar to those obtained from the numerical resolution.
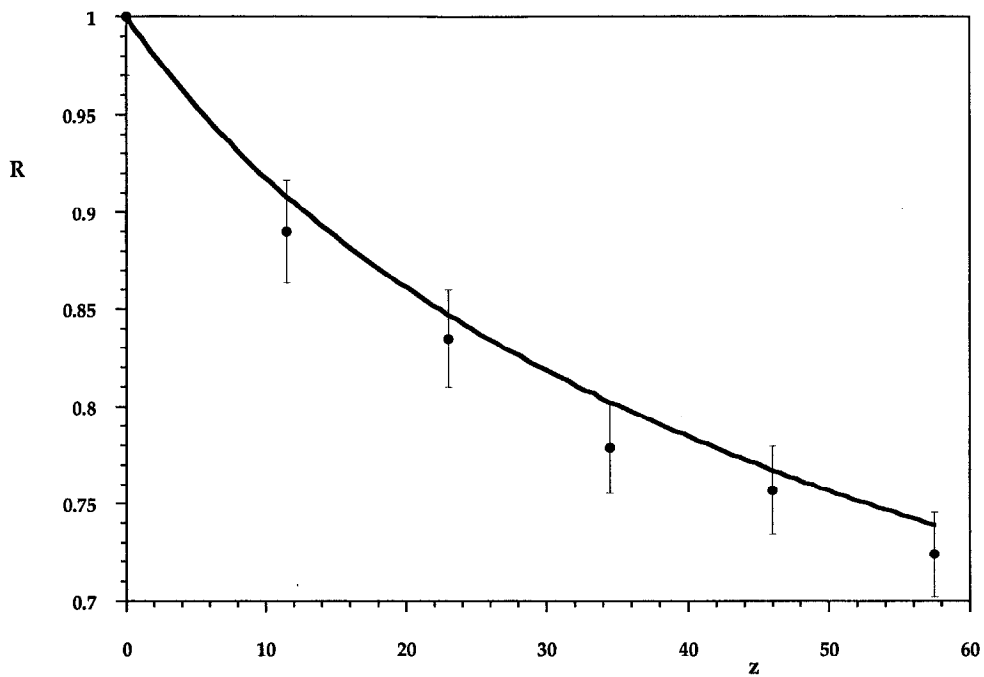
Fig. 11. Comparison in the jet contraction vs z-axis between numerical and experimental results for a pouring of molten oxides where $Re_2 \approx 270$ and $Pe_2 \approx 26\ 500$ ($Fr \approx 24$; $We \approx 340$). (——) Numerical results; (•) experimental points; (♦) error bars (3%).
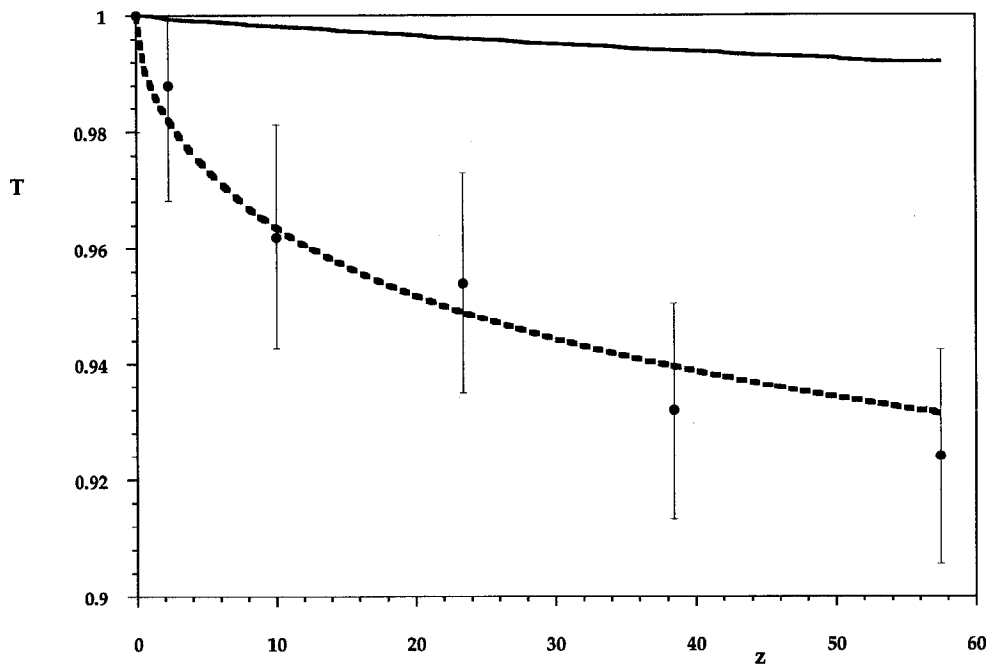
Fig. 12. Comparison in the surface temperature variation vs z-axis between numerical and experimental results for a pouring of molten oxides where $Re_2 \approx 270$ and $Pe_2 \approx 26\ 500$ ($Fr \approx 24$; $We \approx 340$). Numerical model: (– – –) surface temperature; (——) mean temperature. (•) Experimental results; (♦) error bars (2%).

CONCLUSION

The dynamics and thermal states of the molten material can be accurately predicted using the numerical approach, provided that the body is assumed to be opaque. The numerical model makes it easier to access characteristic quantities throughout the jet and to evaluate diameter contraction, velocity profile relaxation and cooling of the pouring jet as it moves away from the nozzle.

The comparison of numerical and experimental diameters shows satisfactory agreement between these two approaches.

The numerical model reveals several interesting results:

—High-temperature jets composed of molten materials reveal significant differences between core and surface temperatures.
—The mean temperature varies slowly moving away from the injection orifice.

The numerical and experimental results both indicate a considerable decrease in the surface temperature on moving away from the nozzle.

It should be noted that the temperature range over which these operations were carried out limits the number of experiments that can be conducted and gives rise to numerous experimental difficulties.

REFERENCES

1. S. Middleman, Profile relaxation in newtonian jets, *Ind. Engng Chem. Fundam.* **3**, 118–122 (1964).
2. C. T. Trang and Y. L. Yeow, Extrudate swell of Newtonian and non Newtonian fluids. The effect of gravitational bodyforce, *J Non-Newtonian Fluid Mech.* **20**, 103–116 (1986).
3. G. Vasudevan and S. Middleman, Momentum, heat, and mass transfer to a continuous cylindrical surface in axial motion, *A.I.Ch.E. J.* **16**, 614–619 (1970).
4. G. Petre and G. Wozniak, Measurement of the variation of interfacial tension with temperature between immiscible liquids of equal density, *Acta Astronautica* **13**, 669–672 (1986).
5. B. J. Meister and G. F. Scheele, Prediction of jet length in immiscible liquid systems, *A.I.Ch.E. J.* **15**, 689–699 (1969).
6. J. S. Vrentas and C. M. Vrentas, Inertia and surface tension effects in Newtonian liquid jets, *Int. J. Multiphase Flow* **8**, 559–564 (1982).
7. T. Tsukiji and K. Takahashi, Numerical analysis of an axisymmetric jet using a streamline coordinate system, *JSME Int. J.* **30**(267), 1406–1413 (1987).
8. E. K. O. Alaoui, Contribution à l'étude des instabilités de jets, injection de liquides et de suspensions dans un autre fluide non-miscible, Thèse de Docteur ès-sciences physiques, Université de Provence, Marseille (1990).
9. L. Tadrist, E. K. O. Alaoui, R. Occelli and J. Pantaloni, Experimental study of liquid jet flowing into another immiscible liquid: a local analysis of the interface, *Exp. Fluids* **12**, 67–75 (1991).
10. G. J. Donnelly and C. B. Weinberger, Stability of isothermal fiber spinning of a Newtonian fluid, *Ind. Engng Chem. Fundam.* **14**, 334–337 (1975).
11. J. C. Chang, M. M Denn and F. T. Geylling, Effects of inertia, surface tension, and gravity on the stability of isothermal drawing of Newtonian fluids, *Ind. Engng Chem. Fundam.* **20**, 147–149 (1981).
12. J. L. Duda and J. S. Vrentas, Fluid mechanics of laminar liquid jets, *Chem. Engng Sci.* **22**, 855–869 (1967).
13. P. Gospodinov, S. Radev and I. Penchev, Velocity profiles and form of a laminar jet in immiscible liquid–liquid systems, *J. Multiphase Flow* **5**, 87–99 (1979).
14. L. Tadrist, Les instabilités de jets en systèmes liquide–liquide, Application aux échangeurs de chaleur à contact direct, Thèse de Doctorat ès-sciences physiques, Université de Provence, Marseille (1987).
15. H. Yu and G. F. Scheele, Laminar jet contraction and velocity distribution in immiscible liquid–liquid systems, *Int. J. Multiphase Flow* **2**, 153–189 (1975).
16. J. R. Fisher and M. M. Denn, A theory of isothermal melt spinning and draw resonance, *A.I.Ch.E. J.* **22**, 236–246 (1976).
17. R. M. Griffith, Velocity, temperature, and concentration distributions during fiber spinning, *Ind. Engng Chem. Fundam.* **3**, 245–250 (1964).
18. M. A. Matovich and J. R. A. Pearson, Spinning a molten threadline—steady state isothermal viscous flows, *Ind. Engng Chem. Fundam.* **8**, 512–520 (1969).
19. Y. T. Shah and J. R. A. Pearson, On the stability of nonisothermal fiber spinning, *Ind. Engng Chem. Fundam.* **11**, 145–153 (1972).
20. J. R. A. Pearson and Y. T. Shah, On the stability of isothermal and nonisothermal fiber spinning of power-law fluids, *Ind. Engng Chem. Fundam.* **13**, 134–138 (1974).
21. S. Radev, R. Rakadjiev, P. Gospodinov and I. Penchev, Numerical method for heat and mass transfer problems for a laminar jet in immiscible liquid–liquid systems, *Proceedings of the First International Conference on Thermal Problems*, pp. 893–902. Pineridge Press, Swansea (1978).
22. R. H. Perry and D. Green, *Perry's Chemical Engineers' Handbook*, 6th Edition, McGraw-Hill International Editions, Chemical Engineering Series, pp 3-264–3-291 (1984).
23. J. J. Froidefond, Etude de la dispersion d'une couche d'oxydes fondus par un jet gazeux, R. R. 334, SEPR Le Pontet (1984).
24. M. M. Anwar, A. Bright, T. K. Das and W. L. Wilkinson, Laminar liquid jets in immiscible liquid systems, *Trans. Instn. Chem. Engrs* **60**, 306–313 (1982)
25. E. F. Nogotov, B. M. Berkovsky and W. J. Minkowycz, *Applications of Numerical Heat Transfer*. Thermal and Fluids Engineering Series, McGraw-Hill, New York (1978).
26. M. Chacha, Modélisation d'un jet de coulée d'oxydes fondus, R. R. 355, SEPR Le Pontet (1991).

APPENDIX: THERMO-PHYSICAL PROPERTIES OF THE FLUID

Density: $\rho_2 = 3500 \text{ kg m}^{-3}$

Heat capacity: $Cp = 1000 \text{ J kg}^{-1} \text{ K}^{-1}$

Thermal conductivity: $\kappa = 4 \text{ W m}^{-1} \text{ K}^{-1}$

Surface tension: $\sigma_{12} = 0.6 \text{ N m}^{-1}$

Dynamic viscosity: $\mu = \mu_0 \exp\left[\dfrac{E}{R_g(T-T_0)}\right]$

$E = 80 \text{ kcal mol}^{-1}$

$\mu_0 = 435 \times 10^{-12} \text{ Pa s at } T_0 = 300°C$